A guide to least-squares reverse time migration for subsalt imaging: Challenges and solutions

Chong Zeng[1], Shuqian Dong[1], and Bin Wang[1]

Abstract

Least-squares reverse time migration (LSRTM) overcomes the shortcomings of conventional migration algorithms by iteratively fitting the demigrated synthetic data and the input data to refine the initial depth image toward true reflectivity. It gradually enhances the effective signals and removes the migration artifacts such as swing noise during conventional migration. When imaging the subsalt area with complex structures, many practical issues have to be considered to ensure the convergence of the inversion. We tackle those practical issues such as an unknown source wavelet, inaccurate migration velocity, and slow convergence to make LSRTM applicable to subsalt imaging in geologic complex areas such as the Gulf of Mexico. Dynamic warping is used to realign the modeled and input data to compensate for minor velocity errors in the subsalt sediments. A windowed crosscorrelation-based confidence level is used to control the quality of the residual computation. The confidence level is further used as an inverse weighting to precondition the data residual so that the convergence rates in shallow and deep images are automatically balanced. It also helps suppress the strong artifacts related to the salt boundary. The efficiency of the LSRTM is improved so that interpretable images in the area of interest can be obtained in only a few iterations. After removing the artifacts near the salt body using LSRTM, the image better represents the true geology than the outcome of conventional RTM; thus, it facilitates the interpretation. Synthetic and field data examples examine and demonstrate the effectiveness of the adaptive strategies.

Introduction

Hydrocarbon explorers have used seismic imaging as a promising tool to discover sweet spots for decades. In a deepwater environment such as the Gulf of Mexico (GOM) in which the cost of drilling is high, seismic images provide essential information for interpreters to analyze the geology in the area of interest. Creating high-quality seismic images that represent the true geology is crucial; otherwise, the imaging artifacts could easily mislead interpreters. When the geologic condition is relatively simple, prestack depth migration often works well and can produce excellent images. Although in some areas, especially where allochthonous salt is involved, the rapidly changing velocity field complicates the reflection of the seismic waves and lowers the quality of the signal received on the surface. The subsequent seismic imaging also suffers from the difficulties of obtaining an accurate migration velocity with insufficient illumination. The salt sheets themselves are usually good traps for oil and gas; thus, the image quality near the salt bodies is often of great interest to the interpreters. Unfortunately, imaging those subsalt areas is particularly challenging. There are a few main reasons. One is that the complex structures significantly distort the wavefield, causing the wavefield to focus in one area and defocus in another area, thus making illumination highly nonuniform on top of the limited acquisition aperture. The other factor is that it is often beyond the capability of conventional imaging algorithms due to the violation of many imaging assumptions. For the first reason, data acquisition technologies have been improved from narrow azimuth to wide azimuth (WAZ), and even full azimuth. Long-offset acquisition is also developed to receive more reflection energy from the deep structures. The acquisition cost, however, also increases almost proportionally to the range of the azimuth and offset. Even with the massive data acquired, seismic images are never perfect due to the intrinsic limitations of the migration algorithms. Therefore, geophysical researchers seek advanced imaging algorithms that can fully take advantages of the available data to improve the image quality in the areas of interest.

Most imaging algorithms, either prestack or poststack, are based on seismic migration using ray approximation or the wave equation. If we assume the earth is a linear system that produces single scattering, then the physical process of the reflection of seismic waves can

[1]TGS-NOPEC Geophysical Company, Houston, Texas, USA. E-mail: chong.zeng@tgs.com; shuqian.dong@tgs.com; bin.wang@tgs.com.

Manuscript received by the Editor 31 October 2016; revised manuscript received 29 December 2016; published online 15 May 2017. This paper appears in *Interpretation*, Vol. 5, No. 3 (August 2017); p. SN1–SN11, 11 FIGS.

http://dx.doi.org/10.1190/INT-2016-0196.1.

be linearly formulated using Born approximation, as follows:

$$\mathbf{d} = \mathbf{L}\mathbf{m}, \tag{1}$$

where $\mathbf{d}$ is the seismic data received on the surface, $\mathbf{m}$ is the earth reflectivity model, and $\mathbf{L}$ is the Born modeling operator that represents how seismic wave propagates and reflects the energy back to the surface. If equation 1 is invertible, the true earth reflectivity can be expressed as

$$\mathbf{m} = \mathbf{L}^{-1}\mathbf{d}. \tag{2}$$

Conventionally, the seismic migration can be formulated as

$$\tilde{\mathbf{m}} = \mathbf{L}^{*}\mathbf{d}, \tag{3}$$

where the migrated image $\tilde{\mathbf{m}}$ is the result of the migration operator $\mathbf{L}^{*}$ applied to the surface data $\mathbf{d}$. The migration operator is an adjoint, rather than the inverse of the modeling operator. Thus, the migration is an approximation of the direct inverse process. Please note we make no assumption on the implementation of the operators so they can be either ray-based or wave equation-based. But the intrinsic difference between $\mathbf{L}^{*}$ and $\mathbf{L}^{-1}$ restricts the capability of conventional migration algorithms regardless of their actual implementation. When complex structures are involved in seismic imaging, this difference is significant enough to introduce artifacts on the seismic image and create pitfalls for interpretation.

Even though experienced interpreters can sometimes recognize artificial events on seismic images, it is still difficult to interpret the true geology because the images are already contaminated by migration artifacts. In many cases, removing those errors after migration without hurting the effective signal is a nontrivial task. In addition, interpreters often demand that the amplitudes on seismic images and the corresponding depth image gathers represent the true reflection coefficients so that other techniques such as amplitude-variation-with-offset (AVO) analysis can be used to evaluate the potential reservoir. To accommodate the needs of advanced interpretation, geophysicists have worked to improve the imaging algorithm by trying to diminish the differences between the migration and inverse so that the image can directly represent the true reflectivity model.

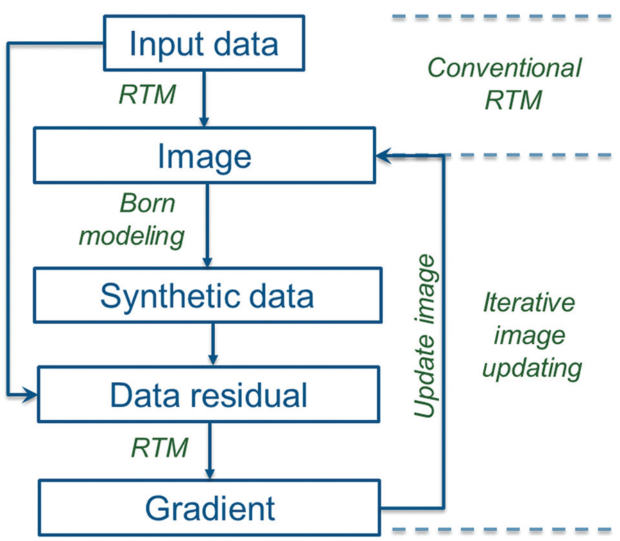

Figure 1. General workflow of LSRTM.

Pioneering works (Schuster, 1993; Nemeth et al., 1999; Duquet et al., 2000) have been described using inversion-based imaging algorithms to overcome the shortcomings of conventional migration methods. By applying a general inverse to equation 1, the true reflectivity can be derived as

$$\mathbf{m} = (\mathbf{L}^{*}\mathbf{L})^{-1}\mathbf{L}^{*}\mathbf{d}, \tag{4}$$

which is equivalent to

$$\mathbf{m} = \mathbf{H}^{-1}\tilde{\mathbf{m}}, \tag{5}$$

and $\mathbf{H}$ is the Hessian represented by

$$\mathbf{H} = \mathbf{L}^{*}\mathbf{L}. \tag{6}$$

It is easy to see that the true reflectivity is the result of applying the Hessian inverse to the conventionally migrated image. In practice, the massive data and model size prohibit the direct solution for the Hessian inverse. Thus, iterative methods such as steepest decent or conjugate gradient are used. The process is implemented by iteratively fitting the synthetic and observed data in a least-squares sense, so that the seismic image is close to the true reflectivity when the observed and synthetic data are matched well. The algorithm is different from conventional migration and is called *least-squares migration (LSM)* by its nature of iterative data fitting in the l_2-norm. In the detailed derivations by Nemeth et al. (1999), the internal modeling and migration engines are based on the Kirchhoff integral. Later on, the works have been extended using various migration implementations in different domains (e.g., Tang, 2009; Dong et al., 2012; Fletcher et al., 2012; Dai et al., 2013). For subsalt imaging, we choose to use the full wave equation for the modeling and migration based on reverse time migration (RTM), so the method is called least-squares RTM (LSRTM).

The iterative inversion process of LSRTM can be generally described using the flowchart in Figure 1. The workflow of LSRTM is very similar to that of full-waveform inversion (FWI), an advanced velocity building technique that has been widely adopted by the seismic industry in the past few decades (Tarantola, 1984; Pratt, 1999; Sirgue and Pratt, 2004; Plessix, 2006). The major difference between LSRTM and FWI is that LSRTM seeks the true earth reflectivity (or impedance), whereas FWI solves for the seismic velocity. Each single iteration of LSRTM is composed of a complete pair of demigration (modeling) and migration. After multiple iterations, the modeled data closely match the input data such that the residuals are insignificant. The reduction of the residual in the time data domain corresponds to the minimization of the differences between the seismic image and the true reflectivity in the depth image domain. When a predefined misfit threshold is achieved, an approximated solution to equation 2 is obtained such that the final output image is close enough to the true earth reflectivity model.

In recent years, LSRTM has been successfully applied to field data for broadband imaging (Zeng et al., 2014b) and other complex structure imaging (e.g., Wong et al., 2011; Zeng et al., 2015; Zhang et al., 2015). Among those applications, LSRTM for subsalt imaging is especially complicated due to some practical limitations such as the velocity error, unknown seismic wavelet, massive computation cost, and second-order artifacts during the iteration (Wang et al., 2013). In the following sections, we analyze the typical problems when applying LSRTM for subsalt imaging and we propose our adaptive solutions. Synthetic and field data examples are implemented to examine the effectiveness of the adaptive strategies. Most of the field data examples are based on acquisition from the GOM, but the method should not be restricted to be applied in any specific area.

Advantages of LSRTM

The RTM technology has been the workhorse for subsalt imaging in the past few decades. It uses the two-way wave equation and naturally handles multipathing and complex reflections. However, it also creates undesired artifacts that have to be identified to avoid any incorrect geologic interpretation. Let us consider a true reflectivity model as shown in Figure 2a. We create some synthetic shot gathers based on it and then migrate the surface data to generate an RTM image (Figure 2b). The input data are composed of 190 shots with a 6 km virtually towed streamer. The source wavelet is an Ormsby wavelet of 1–2–18–22 Hz. By comparing the true model and the RTM image, we can see the differences are significant. First, the overall amplitudes of the RTM image and the corresponding depth image gathers are far from that of the true reflectivity. This makes any amplitude-based analysis (such as AVO) almost impossible. Second, the RTM image contains strong migration swing artifacts near the salt body. The conflicting dips of the swing artifacts and the true sediments confuse the interpreters. In the area close to the salt body, it is difficult to trace the horizons due to the strong artifacts. The image of the vertical salt flank is not clear. Finally, the RTM image is band limited due to the wavelet effect introduced in migration and contains side lobes of the source wavelet.

Of course, an experienced interpreter can easily point out the artifacts on the above RTM image. However, we would like to emphasize that the case illustrated by Figure 2 is probably still much simpler compared with the field data applications. The input data are noise-free synthetics created by the acoustic-wave equation. The

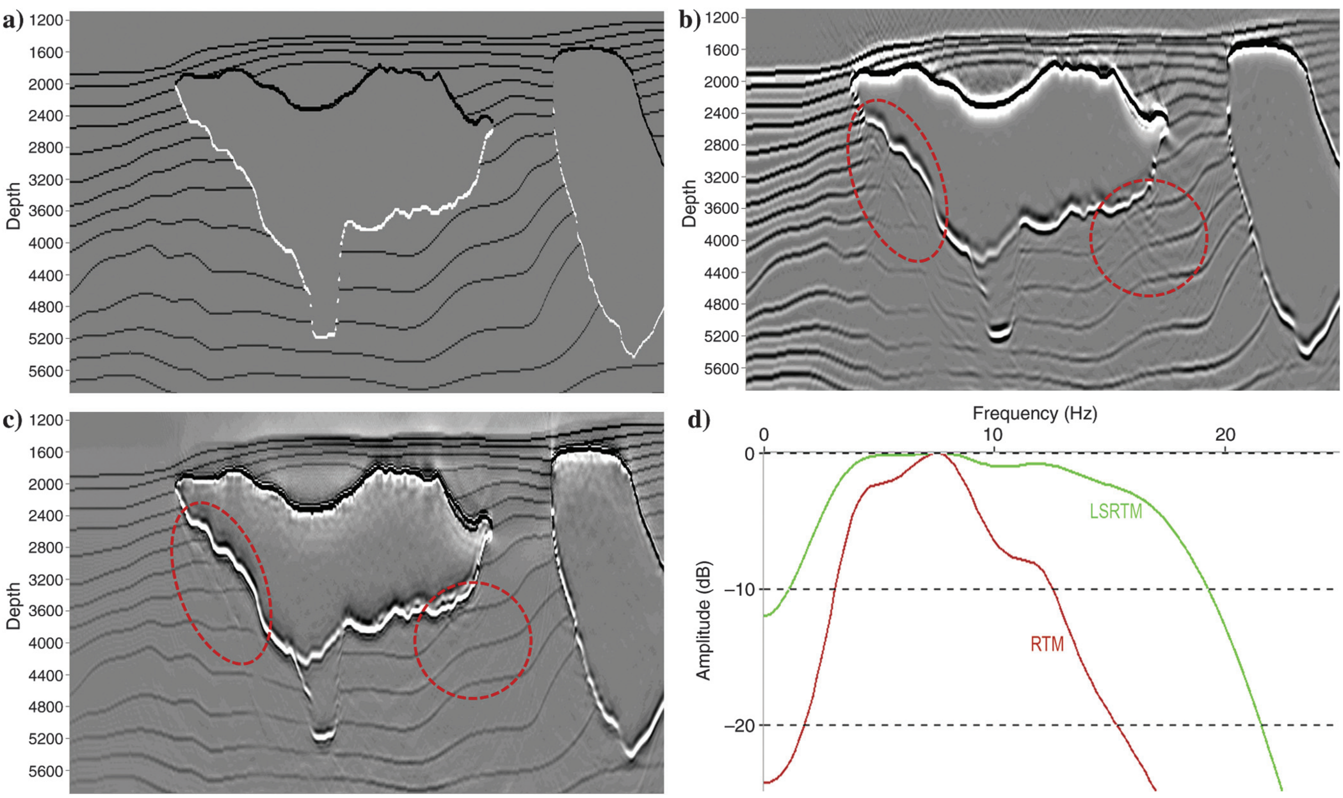

Figure 2. (a) True reflectivity model, (b) conventional RTM image, and (c) LSRTM image of the synthetic salt model based on a GOM survey. (d) Comparison of the amplitude spectra of the RTM and LSRTM images.

surface data coverage is abundant. The migration velocity model is perfect even in the shadow area where the illumination is poor. In contrast, the field data are always complicated by multiples, converted waves, and many other factors such as attenuation. The migration velocity is never perfect. Also, the migration job has to restrain the upper bound frequency due to the massive computation cost in large 3D projects.

Compared with the RTM image, LSRTM gives a superior result (Figure 2c), which is very close to the true solution, using exactly the same input data and velocity model. The amplitude spectra of the RTM and LSRTM image (Figure 2d) confirm that the wavelet effect has been removed by LSRTM as a natural 3D deconvolution. The advantages of the LSRTM can be summarized as follows (Zeng et al., 2014a):

1) Amplitudes are balanced better by revealing weak signals and pushing the image toward the true-reflectivity model.
2) Migration artifacts caused by acquisition footprints or nonuniform illumination are reduced.
3) Spatial resolution is increased by enriching the low frequencies and suppressing the image side lobes.
4) The signal-to-noise ratio (S/N) is enhanced by improving the images of steep dips or other complex structures.

An important feature of LSRTM is its unique internal mechanism to remove the migration artifacts. In field data applications, seismic imagers have tried various postmigration techniques to reduce the artifacts on the RTM image. Some are performed by filtering (e.g., Guitton et al., 2007; Zhang and Sun, 2009), and others are performed by using advanced stacking methods (e.g., Liu et al., 2009; Sanchis and Hanssen, 2011). Unfortunately, most of them inevitably hurt the signal when the artifacts share similar characteristics with the effective signal. Figure 3a shows an example that is challenging for the postmigration process. It is an RTM image based on a set of data from WAZ acquisition in the GOM. The image shows a group of faults on the left portion and a lot of swing artifacts near the salt boundary. The swing artifacts look very similar to the faults. Conventional postmigration processing that can remove the artifacts will likely degrade the image in the fault zone. Instead, LSRTM removes the artifacts without hurting the effective signal in a completely different way. It first creates demigrated surface data based on the initial RTM image and calculates the differences between the modeled and input (field) data. All true structures such as the sediments and salt boundary will create synthetic reflections that match the real events on the input shot gathers. The swing artifacts after demigration, however, will become spurious events in the modeled data that has no corresponding events in the input data because the real earth contains no such artificial reflectors. When calculating the data residual between the input and modeled data, the matched events vanish and the spurious events become inverse polarity wiggles. After migrating the residual again, the inverse polarity wiggles in the data domain have been mapped to the image domain to be the inverse polarity events on the LSRTM gradient (Figure 3b). The summation

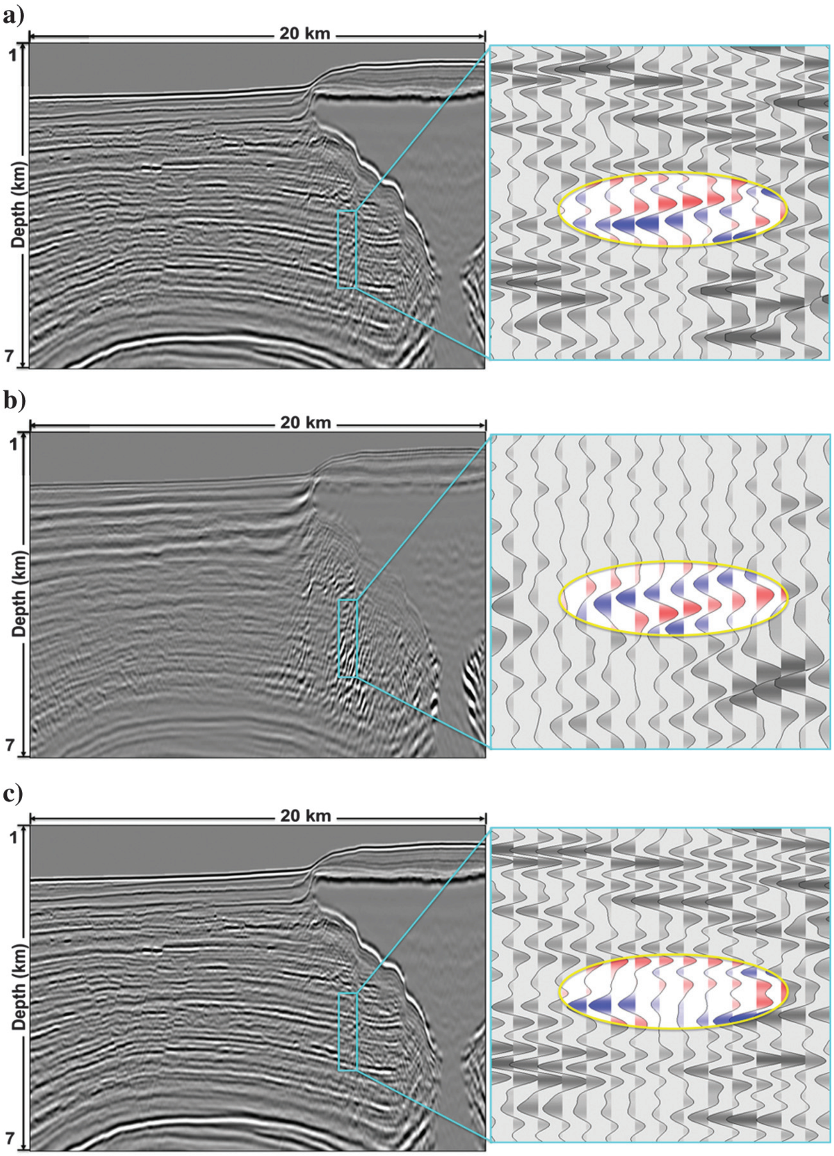

Figure 3. (a) Conventional RTM image, (b) LSRTM gradient of the first iteration, (c) LSRTM image after updating. The steeply dipping fault planes are enhanced, whereas the swing artifacts (magnified on the right side) are canceled out regardless of their similar dipping and geometric pattern.

of the initial RTM image and the gradient (after weighting by the proper step length) naturally cancels the swing artifacts and yields a clean image (Figure 3c). The real signals, such as faults, are maintained because the gradient is in phase with the original image due to the vanished residual in the data domain. It should be noted that in this whole procedure of LSRTM, there is no need to predefine which event is true or artificial. Hence, the differentiation of real signals and artifacts is handled automatically. This reduces the possibility of selecting wrong events for noise removal due to human manipulation in conventional postmigration processing. In field data applications, this modeling-based noise cancelation is performed by multiple iterations so that the artifacts are gradually reduced.

Practical challenges of LSRTM for subsalt imaging

In time-domain implementations of LSRTM, the modeling process requires a band-limited source wavelet to generate the modeled data. Usually, the source wavelet can be obtained by analyzing the source signature of the input data. In practice, the wavelet is complicated and changes the phase during propagation. Other noises in the data such as ghosts also distort the wavelet. In LSRTM modeling, the seismic image is usually used as the reflectivity to be convolved with the source wavelet. The side lobes on the image are blended with the original source wavelet and create complicated wiggles on the modeled data. In most cases, direct subtraction of the input and modeled data causes a very slow convergence of the inversion due to the improper match of the synthetic and field wavelet.

On the other side, the amplitudes of the modeled data are usually not reliable due to the lack of considering attenuation and elastic conversion during wave propagation. It is often found that the inversion is trapped to most update the shallow images because the shallow reflections are easy to match. The data residuals of the shallow reflections are more pronounced than those from the deep reflections. This causes different convergence rates for the shallow part (e.g., top salt) and the deep part (e.g., the subsalt area) of the image. Unless a well-designed regularization term is added to the inversion, getting a satisfactory result for the subsalt area typically needs a lot of iterations. When applying LSRTM for large 3D projects focusing on subsalt improvements, the slow convergence rate can make the computation cost significantly high. More importantly, the different convergence rates for the shallow and deep parts increase the risk of inversion divergence. When the subsalt area reaches the optimum point, the shallow part could be overmatched due to the noise in the field data.

Besides the wavelet and amplitude issues of modeling, the error in migration velocity is probably the most serious issue in subsalt imaging. The flowchart in Figure 1 shows that each iteration of LSRTM needs a set of demigration and migration. It also implies that the seismic velocity has to be taken into account as an input parameter for the migration and demigration. Because there is no place in the workflow to modify the migration velocity, any error in the velocity field will remain in the inversion and could be amplified after many iterations. For this reason, the theory of LSRTM (or any implementation of LSM) assumes perfect migration velocity to assure the convergence. However, this is unrealistic in field data applications because building a velocity model from field data is never an easy task. Especially in the subsalt area, the salt sheet acts as a high-velocity lens that can sharply change the propagation direction of the incident seismic waves and cause poor illumination in the subsalt area. Neither conventional tomography nor FWI can handle this situation without caution. The velocity uncertainty in the subsalt area is usually higher than that above the salt. The salt canopy reflects most energy back to the surface; thus, the S/N below the salt is usually very low. The situation is even worse in areas containing several closely located salt bodies. For subsalt imaging, obtaining a perfect velocity seems an open question (Etgen et al., 2014). An interesting study by Albertin and Zhang (2014) also shows that imaging errors can happen even with the perfect velocity when a complex salt body is involved. If we directly apply LSRTM without considering the error in the velocity field, the inversion can converge to an erroneous image (Huang et al., 2014; Hou and Symes, 2016).

Preconditioning in the data domain

In this section, we propose some data-adaptive strategies to address the practical issues that are related to subsalt imaging using LSRTM. These strategies not only ensure the convergence of the inversion but also improve the efficiency of the algorithm. Simply speaking, our preconditioning in the data domain uses forward modeling to guide processing the input data to either speed up the convergence, enhance the weak signal, or make our final image toward true amplitude reflectivity. Depending on the imaging objectives, different types of preconditioning can be used (e.g., Dutta et al., 2017). If the primary objective is true amplitude reflectivity, the matching filter idea based on approximate Hessian (Guitton, 2004; Wang et al., 2013) can be effectively applied in the data domain. If our primary imaging objective is structure imaging and fast convergence, we are not intended to retrieve the true reflectivity in a single step. Instead, the strategies are focused to tackle the most important problems in field data applications so that we can create easily interpretable images using the best available velocity models in an efficient way.

To minimize the side effects of inaccurate source wavelets in data subtraction, we apply a matching filter to the modeled data so the wiggles of the synthetic and field data are directly comparable. If the original objective function is formulated as

$$J(\mathbf{m}) = \|\mathbf{Lm} - \mathbf{d}\|_2. \quad (7)$$

Then the improved objective function is

$$\mathcal{J}(\mathbf{m}) = \|\mathbf{p_m}(\mathbf{Lm}) - \mathbf{p_f}\mathbf{d}\|_2, \tag{8}$$

where $\mathbf{p_m}$ is a filter applied to match the forward-modeled data with the observed data and $\mathbf{p_f}$ is the preprocessing operator applied to the observed field data. The specific implementation of the preprocessing operator is case dependent. For marine acquisition, the input data should be preprocessed to remove the ghost effect (Dong et al., 2014). After that, we scale the root-mean-square amplitude of the modeled data using a sliding-window-based gain control with respect to the input data (Zeng et al., 2015). The purpose of this scaling is to make the amplitudes of the synthetic data consistent with that of the input data so that direct subtraction is feasible.

To further help control the quality of the data residual computation, we use a windowed crosscorrelation coefficient to measure the level of match between the modeled and input data. We name these correlation coefficients "confidence level" because they quantitatively tell which part of the data matches well or poorly. Specifically, the confidence level is calculated as follows:

$$c_i = \frac{\sum_{ix=-h}^{h}\sum_{it=-l}^{l}(d_i-\overline{d})(u_i-\overline{u})}{\sqrt{\sum_{ix=-h}^{h}\sum_{it=-l}^{l}(d_i-\overline{d})^2}\sqrt{\sum_{ix=-h}^{h}\sum_{it=-l}^{l}(u_i-\overline{u})^2}}, \tag{9}$$

where d and u are the input and synthetic samples, respectively. The h and l are the half-window size along the spatial and temporal directions. The bar denotes the arithmetic average.

We borrow the idea proposed by Luo and Hale (2014) to use dynamic warping to address the minor velocity error in the subsalt area. The dynamic warping was originally designed to shift the samples of a time signal (such as the human voice) with respect to a reference for speech recognition (Sakoe and Chiba, 1978; Müller, 2007). It is later introduced by Hale (2013) to estimate the shifts between two seismic images. In LSRTM, the arrival time of synthetic surface data after demigration highly depends on the velocity model. The inaccurate velocity causes the shifts between the modeled and input wiggles. This misalignment introduces false events in the residual and generates secondary swing artifacts on the LSRTM gradient. The shifts between the modeled and input wiggles are nonlinear and vary with offset and time. Figure 4 illustrates a modeled shot gather during LSRTM when velocity error occurs. The colors overlaid on the wiggles represent the degree of misalignment between the modeled and input wiggles. It shows that the far offset and deep reflections are usually more prone to the velocity errors than the near offset and shallow data. Dynamic warping directly estimates the shifts between the two data sets, so we can realign the wiggles without knowing the exact velocity difference.

It is noteworthy that dynamic warping should be applied to the input data rather than to the modeled data (Luo and Hale, 2014). Because the modeled data are created by the demigration process using the same velocity model that was used for previous migration, the synthetic mapping from the data domain to the image domain and vice versa is self-consistent. However, this is not true for the field data. The field data can be considered as a result of modeling using the true earth reflectivity and the accurate (but unknown) earth velocity model. Therefore, the field data are consistent with the true-earth velocity rather than the estimated (but erroneous) migration velocity. For field data applications, we have no means to get the perfect velocity but have to use the estimated migration velocity with certain degrees of inaccuracy. In this case, adjusting the field data such that it is aligned to the synthetic data is a practical choice.

Using dynamic warping to align the modeled and input data promotes the inversion to converge to the true solution. The warped input data are equivalent to the results from the modeling based on true earth reflectivity and the derived migration velocity. LSRTM seeks only for the true earth reflectivity, but the true earth velocity is also unknown. By directly fitting the raw input and synthetic data, the inversion contains two unknowns (true reflectivity and true velocity) but searches for only one of them. The ignorance of velocity updating makes the inversion converge to a solution deviated from the global minima of the two-parameter misfit function. On the contrary, fitting the warped input and synthetic data eliminates the involvement of the true earth velocity and leaves the true earth reflectivity as the only unknown for solution. It adjusts the problem to a single-parameter optimization and simplifies the inversion.

The confidence level in equation 9 is used to evaluate the effectiveness of the data preconditioning such as dynamic warping and amplitude correction. Fig-

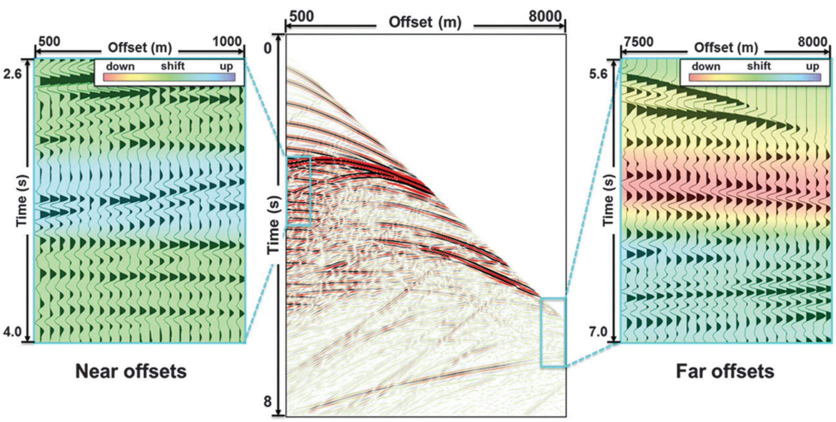

Figure 4. A synthetic example on data shifting caused by velocity errors. The colors overlaid on the wiggles represent the degree of misalignments between the modeled and input wiggles.

ure 5 shows the modeled and input data after processing. We apply the amplitude matching to the synthetic data and the dynamic warping to the input data. The increase of confidence level in the deep reflections and far-offset range (Figure 6) indicates that the input and synthetic wiggles are now better aligned for the LSRTM residual computation. After the preconditioning, the synthetic and input data are directly comparable, so residual data can be computed by subtraction to get the l_2-norm in equation 8.

The confidence level is not only used as a quality control tool but also can serve the inversion as an adaptive residual preconditioning to balance the convergence rates between the shallow and deep images. It is often found that LSRTM needs many iterations to produce notable improvements in the subsalt areas. This is primarily because the data quality or S/N corresponding to the subsalt reflectors is not as good as the shallow reflections. Some strong reflectors, such as the water bottom and salt boundaries, dominate the amplitude of the surface data. When calculating the data residual, those events are strong enough to bury the weak subsalt reflections. This means at the beginning of the iteration, the algorithm will primarily update the images corresponding to those strong reflectors. In practice, this is less efficient and sometimes unnecessary because the initial RTM images for the strong reflectors are already good enough for interpretation. The weak events such as the subsalt reflections or the sediments adjacent to the salt body are critical to the interpretation but cannot get sufficiently updated. To make the LSRTM algorithm automatically focus on the weak signals, we can apply the confidence level as an inverse weighting to precondition the residual data. Because the strong reflection events usually pose a higher confidence level due to the good match between the modeled and input data, they are automatically dimmed down in the residual after this inverse weighting. Meanwhile, the weak events are enhanced in the residual so that the image update can be automatically emphasized in the subsalt areas. This automatic residual preconditioning also helps suppress those salt-related artifacts in LSRTM (Zeng et al., 2016). We found this adaptive weighting to be significantly efficient for subsalt applications. Interpretable images in the area of interest can be obtained within only a few iterations with the speed up of the subsalt convergence.

Synthetic tests

We build a synthetic salt model shown in Figure 7a to examine the effectiveness of the adaptive strategies for LSRTM. We manually add minor errors in the migration velocity to simulate the case in field data processing. The errors vary from 1% to 6% with the increase in depth and change laterally with respect to the position of the salt body (Figure 7b). Figure 8 shows the outputs of LSRTM with and without applying the adaptive strategies after one iteration. For the result without applying the adaptive strategies (Figure 8a), the shallow part (the velocity error is less than 2%) is not focused well. The image seems acceptable because the overall velocity in

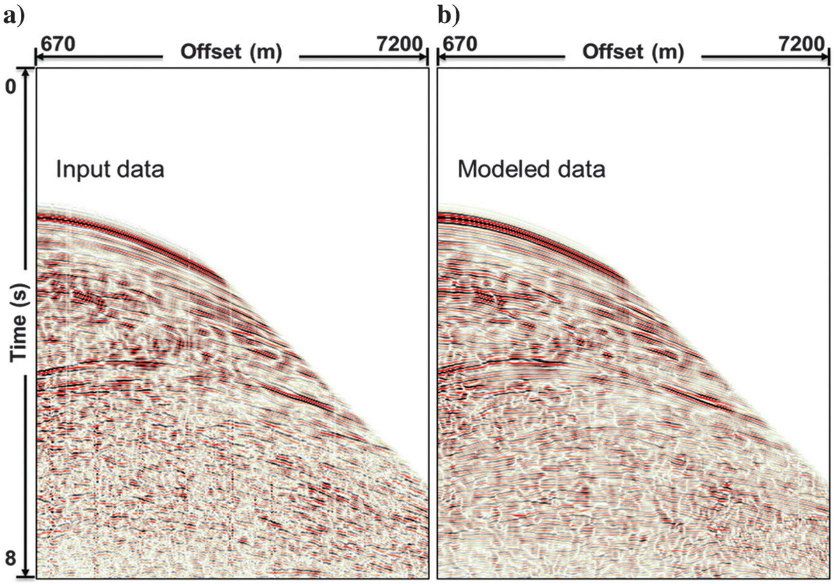

Figure 5. (a) A real shot gather extracted from a survey based in GOM versus (b) the modeled shot gather during the first iteration of LSRTM.

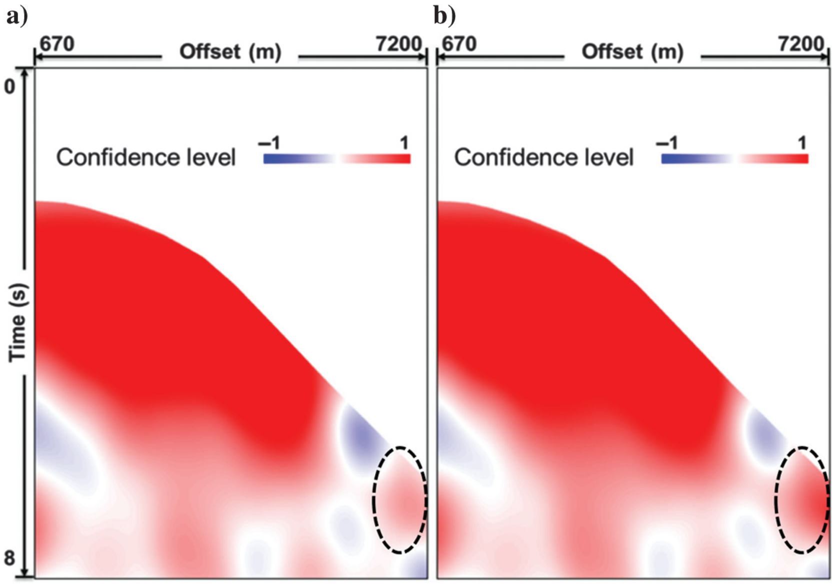

Figure 6. The confidence level (a) before and (b) after adaptive data adjusting. Changes are observed in the far-offset range (marked by the dashed ovals).

the shallow is low and the 2% error mainly influences high-frequency or short-wavelength components during the imaging. The low-frequency components can still correctly position the reflectors, but they are out of phase with the high-frequency components. Without dynamic warping, the error in high frequencies remains in the LSRTM iteration and causes a problem similar to "cycle skipping" in FWI. By automatically stretching or compressing the wiggles of input data using dynamic warping, the high-frequency errors are compensated such that the image is focused (Figure 8b).

In the subsalt area where the background velocity is high and the error is also relatively large, the absolute error of the velocity is significant enough to distort the wavefield in the low and high frequencies. The LSRTM result without applying the adaptive strategies (Figure 8a) shows broken events in the subsalt area. The diffraction style migration tails in the broken area indicate that the inversion failed to converge. After applying the adaptive strategies, the subsalt area events are more continuous. Although it is still different from the true solution, the collapse of the migration tail can guide the interpreters to trace the horizon and avoid the possibility of erroneous fault recognition.

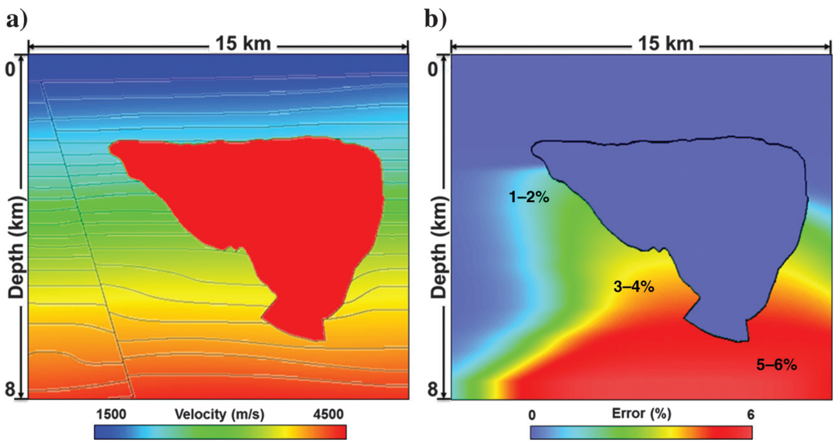

Figure 7. (a) The accurate velocity model overlaid with true reflectivity. (b) The migration velocity containing error overlaid with the true reflectivity.

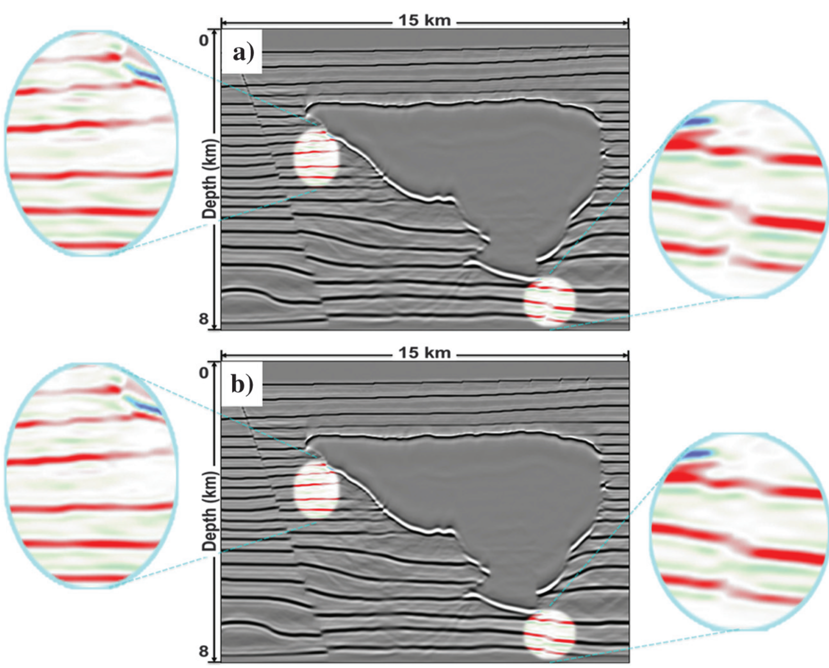

Figure 8. The LSRTM image after one iteration (a) without and (b) with applying the adaptive strategies.

Field data examples

The adaptive LSRTM shows great potential for practical subsalt imaging. We have successfully practiced this technology with large volumes of seismic data acquired in the GOM. Here, we provide two field data examples to illustrate how adaptive LSRTM can help the subsalt interpretation.

The first set of field data is called Freedom 3D WAZ. The survey is a typical WAZ acquisition with 8 km long multicable streamers near the Mississippi Canyon in the GOM. Figure 9a shows an inline section of the 3D RTM image volume. A huge salt body covers almost the entire area of interest. On the left portion of the image (area A on Figure 9a), there are some artifacts parallel to the salt boundary. These artifacts are conventionally referred to as a salt "halo" because they appear as a repeated artificial salt boundary. The strong halo artifacts are blended with the images of the sediment layers and show conflicting dips for interpretation. On the right side of the image (area B), the image quality is limited. The canopy-shaped base of salt acts like a convex mirror to reflect most of the seismic energy back to the surface and leaves very poor illumination in the subsalt area. The discontinuous image of the base of salt also indicates that there are possible velocity errors around the salt body. The low S/N in the subsalt introduces difficulties to recover the geologic history for further analysis. After the adaptive LSRTM (Figure 9b), the halo artifacts in area A are removed to show clear geologic contacts between the sediment layers and the base of salt. In area B, the weak signals are recovered such that tracing the horizons is much easier than before. The overall comparison of the conventional RTM and adaptive LSRTM images suggests that the adaptive LSRTM offers significant subsalt enhancements and produces interpretation favorable results.

We further extend the success of the adaptive LSRTM on subsalt imaging using the Patriot 3D WAZ data set. The data set is also from the GOM but with a different survey direction. The geologic condition of Patriot is more complex than the previous Freedom area. On the depth slice down to 5600 m of the conventional RTM volume (Figure 10a), we observe that the sediment area is surrounded by two closely located salt domes. This causes typical imaging problems due to the complexity of the wavefield near the steeply dipping salt flanks. Strong migration swings appear in the marked area A and contaminate the image near the salt body. On the marked area B, the salt halo can easily mislead the interpreters to be considered as a fault plane. After one iteration of adaptive LSRTM, the migration swings are reduced and the strong halo artifacts are suppressed to show the sharp geologic contacts near the salt body. Detailed image improvements can be found on the inline section of the 3D image volumes (Figure 11). After adaptive LSRTM, the migration swings (Figure 11a) on the middle part of the image are canceled (Figure 11b) so as to eliminate the confusion of conflict dips for inter-

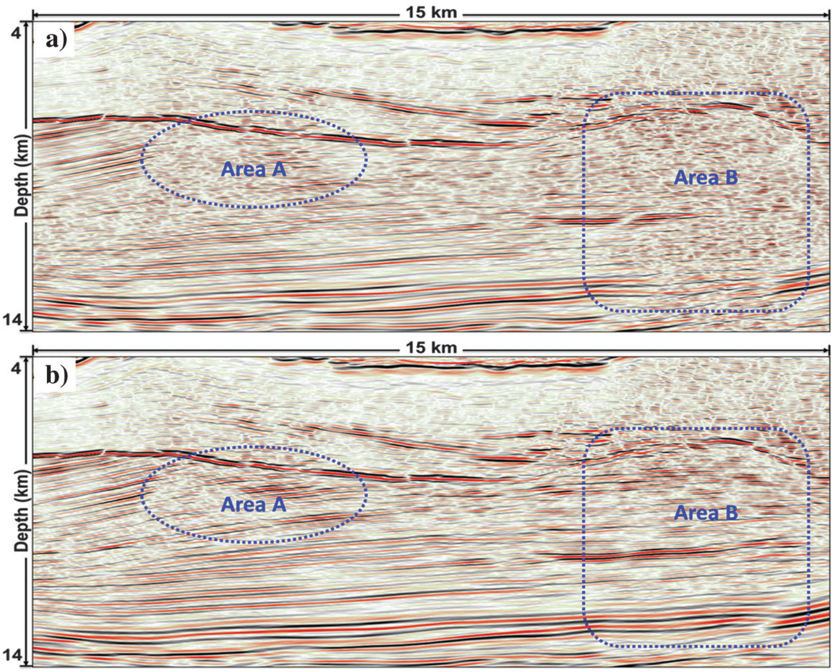

Figure 9. (a) Conventional RTM image and (b) adaptive LSRTM image from the Freedom 3D WAZ data. The RTM and LSRTM volumes are applied exactly same postmigration processing such as low cut filtering and salt muting.

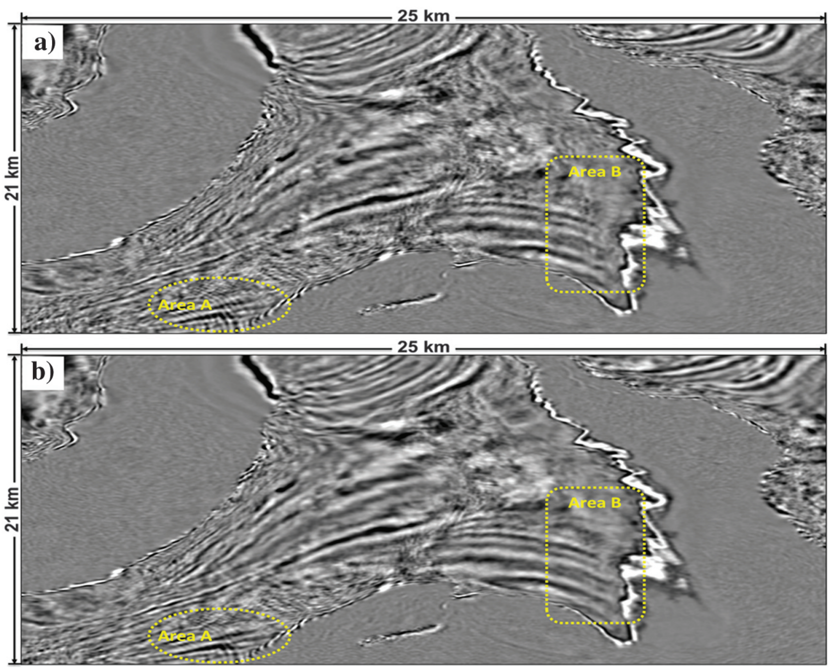

Figure 10. Depth slice down to 5600 m of the (a) conventional RTM image and (b) adaptive LSRTM image of the Patriot 3D WAZ data. The RTM and LSRTM volumes have applied exactly the same postmigration processing for cosmetic purpose.

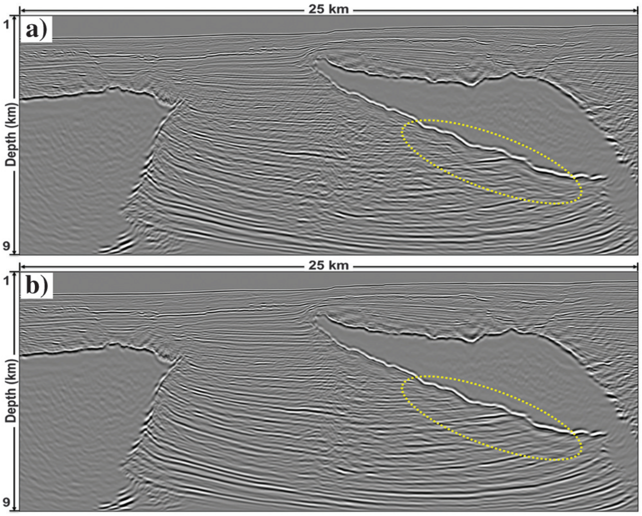

Figure 11. Inline section of the (a) conventional RTM image and (b) adaptive LSRTM image of the Patriot 3D WAZ data.

pretation. On the conventional RTM image (Figure 11a), the low-frequency halo artifacts near the overhung salt body obscure the effective signals from the sediments. After adaptive LSRTM (Figure 11b), the halo artifacts are suppressed so the weak sediment layers adjacent to the salt are now revealed. The quality of the image has been substantially improved after the adaptive LSRTM to facilitate the interpretation.

Conclusions

LSRTM refines a conventional RTM image toward true reflectivity through least-squares inversion. Despite the mathematical beauty of the theory, applying LSRTM to field data under complex geologic conditions is still challenging. We have discussed the practical issues when applying LSRTM to subsalt imaging. Adaptive solutions are provided to address those practical issues. Specifically, matching filters are used for preconditioning in the data domain. We use dynamic warping to compensate the minor errors in migration velocity, so the modeled and input data are consistent with the actual used velocity model. To boost weak signals and speed up convergence, the crosscorrelation-based confidence level is used to control the quality of the residual computation. It is further used as an inverse weighting to precondition the data residual to stabilize the inversion and improve the efficiency of the algorithm. With the adaptive strategies, LSRTM can tolerate minor migration velocity errors and converges in only a few iterations to yield notable subsalt improvements. The synthetic and field data examples show that adaptive LSRTM can significantly improve the quality of subsalt image with relatively low computation cost. Many common artifacts such as migration swings and salt halos are automatically removed by adaptive LSRTM, so the final image is more geologically favorable than that of conventional RTM.

Acknowledgments

We highly appreciate J. Ji for the data preparation, Z. Zhang, D. Teixeria for the GPU programming, and C. VanSchuyver for the manuscript proofreading. We are grateful to Z. Wu, D. Armentrout, L. Li, and T. Kim for their great efforts in the field data testing. We thank G. Rodriguez, H. Roende, and Z. Li for continuous support as well as the TGS management for permission to publish. The GOM field data are courtesy of TGS and WesternGeco. Finally, we thank K. J. Marfurt and A. Mao for their kind invitation, as well as G. Dutta, Y. Liu, J. Hou, and an anonymous reviewer for their constructive comments.

References

Albertin, U., and L. Zhang, 2014, Migration optimization through local phase alignment of partial migration images: 84th Annual International Meeting, SEG, Expanded Abstracts, 3769–3773.

Dai, W., Y. Huang, and G. T. Schuster, 2013, Least-squares reverse time migration of marine data with frequency-selection encoding: Geophysics, **78**, no. 4, S233–S242, doi: 10.1190/geo2013-0003.1.

Dong, S., J. Cai, M. Guo, S. Suh, Z. Zhang, B. Wang, and Z. Li, 2012, Least-squares reverse time migration: Towards true amplitude imaging and improving the resolution: 82nd Annual International Meeting, SEG, Expanded Abstracts, doi: 10.1190/segam2012-1488.1.

Dong, S., C. Zeng, H. Masoomzadeh, and B. Wang, 2014, Deghosted least-squares RTM: Image domain broadband solution for complex structures: 76th Annual International Conference and Exhibition, EAGE, Extended Abstracts, Th ELI1 11, doi: 10.3997/2214-4609.20141449.

Duquet, B., K. J. Marfurt, and J. A. Dellinger, 2000, Kirchhoff modeling, inversion for reflectivity, and subsurface illumination: Geophysics, **65**, 1195–1209, doi: 10.1190/1.1444812.

Dutta, G., M. Giboli, C. Agut, P. Williamson, and G. T. Schuster, 2017, Least-squares reverse time migration with local radon-based preconditioning: Geophysics, **82**, no. 2, S75–S84, doi: 10.1190/geo2016-0117.1.

Etgen, J. T., I. Ahmed, and M. Zhou, 2014, Seismic adaptive optics: 84th Annual International Meeting, SEG, Expanded Abstracts, 4411–4415.

Fletcher, R. P., S. Archer, D. Nichols, and W. Mao, 2012, Inversion after depth imaging: 82nd Annual International Meeting, SEG, Expanded Abstracts, doi: 10.1190/segam2012-0427.1.

Guitton, A., 2004, Amplitude and kinematic corrections of migrated images for non-unitary imaging operators: Geophysics, **69**, 1017–1024, doi: 10.1190/1.1778244.

Guitton, A., B. Kaelin, and B. Biondi, 2007, Least-squares attenuation of reverse-time-migration artifacts: Geophysics, **72**, no. 1, S19–S23, doi: 10.1190/1.2399367.

Hale, D., 2013, Dynamic warping of seismic images: Geophysics, **78**, no. 2, S105–S115, doi: 10.1190/geo2012-0327.1.

Hou, J., and W. W. Symes, 2016, Accelerating extended least-squares migration with weighted conjugate gradient iteration: Geophysics, **81**, no. 4, S165–S179, doi: 10.1190/geo2015-0499.1.

Huang, Y., G. Dutta, W. Dai, X. Wang, G. T. Schuster, and J. Yu, 2014, Making the most out of least-squares migration: The Leading Edge, **33**, 954–956, 958–960, doi: 10.1190/tle33090954.1.

Liu, G., S. Fomel, L. Jin, and X. Chen, 2009, Stacking seismic data using local correlation: Geophysics, **74**, no. 3, V43–V48, doi: 10.1190/1.3085643.

Luo, S., and D. Hale, 2014, Least-squares migration in the presence of velocity errors: Geophysics, **79**, no. 4, S153–S161, doi: 10.1190/geo2013-0374.1.

Müller, M., 2007, Information retrieval for music and motion: Springer.

Nemeth, T., C. Wu, and G. T. Schuster, 1999, Least-squares migration of incomplete reflection data: Geophysics, **64**, 208–221, doi: 10.1190/1.1444517.

Plessix, R. E., 2006, A review of the adjoint-state method for computing the gradient of a functional with geophysical applications: Geophysical Journal International, **167**, 495–503, doi: 10.1111/j.1365-246X.2006.02978.x.

Pratt, R. G., 1999, Seismic waveform inversion in the frequency domain — Part 1: Theory and verification in a physical scale model: Geophysics, **64**, 888–901, doi: 10.1190/1.1444597.

Sakoe, H., and S. Chiba, 1978, Dynamic programming algorithm optimization for spoken word recognition: IEEE Transactions on Acoustics, Speech, and Signal Processing, **26**, 43–49, doi: 10.1109/TASSP.1978.1163055.

Sanchis, C., and A. Hanssen, 2011, Enhanced local correlation stacking method: Geophysics, **76**, no. 3, V33–V45, doi: 10.1190/1.3552687.

Schuster, G. T., 1993, Least-squares cross-well migration: 63rd Annual International Meeting, SEG, Expanded Abstracts, 110–113.

Sirgue, L., and R. G. Pratt, 2004, Efficient waveform inversion and imaging: A strategy for selecting temporal frequencies: Geophysics, **69**, 231–248, doi: 10.1190/1.1649391.

Tang, Y., 2009, Target-oriented wave-equation least-squares migration/inversion with phase-encoded Hessian: Geophysics, **74**, no. 6, WCA95–WCA104, doi: 10.1190/1.3204768.

Tarantola, A., 1984, Inversion of seismic-reflection data in the acoustic approximation: Geophysics, **49**, 1259–1266, doi: 10.1190/1.1441754.

Wang, B., S. Dong, and S. Suh, 2013, Practical aspects of least-squares reverse time migration: 75th Annual International Conference and Exhibition, EAGE, Extended Abstracts, We P09 02, doi: 10.3997/2214-4609.20131000.

Wong, M., S. Ronen, and B. Biondi, 2011, Least-squares reverse-time migration/inversion for ocean bottom data: A case study: 81st Annual International Meeting, SEG, Expanded Abstracts, 2369–2373.

Zeng, C., S. Dong, J. Mao, and B. Wang, 2014b, Broadband least-squares reverse time migration for complex structure imaging: 84th Annual International Meeting, SEG, Expanded Abstracts, 3715–3719.

Zeng, C., S. Dong, and B. Wang, 2014a, Least-squares reverse time migration: Inversion-based imaging toward true reflectivity: The Leading Edge, **33**, 962–968, doi: 10.1190/tle33090962.1.

Zeng, C., S. Dong, and B. Wang, 2016, Adaptive least-squares RTM with applications to subsalt imaging: The Leading Edge, **35**, 253–257, doi: 10.1190/tle35030253.1.

Zeng, C., S. Dong, Z. Wu, J. Ji, D. Armentrout, and B. Wang, 2015, Adaptive least-squares RTM and application to Freedom WAZ subsalt imaging: 85th Annual International Meeting, SEG, Expanded Abstracts, 4059–4064.

Zhang, Y., L. Duan, and Y. Xie, 2015, A stable and practical implementation of least-squares reverse time migration: Geophysics, **80**, no. 1, V23–V31, doi: 10.1190/geo2013-0461.1.

Zhang, Y., and J. Sun, 2009, Practical issues in reverse time migration: True amplitude gathers, noise removal and harmonic source encoding: First Break, **26**, 29–35.

Biographies and photographs of authors are not available.